Journal of Materials Chemistry A



PAPER

View Article Online
View Journal | View Issue



Cite this: J. Mater. Chem. A, 2018, 6, 17426

Impact of cesium on the phase and device stability of triple cation Pb-Sn double halide perovskite films and solar cells†

Gabriella A. Tosado, Yi-Yu Lin, Erjin Zheng 📵 and Qiuming Yu 📵 *

Triple cation Cs/methylammonium (MA)/formamidinium (FA) and double halide Br/I lead perovskites improved the stability and efficiency of perovskite solar cells (PVSCs). However, their effects on alloyed Pb–Sn perovskites are unexplored. In this work, perovskite thin films with the composition Cs_x(MA_{0.17}FA_{0.83})_{1-x}Pb_{1-y}Sn_y(I_{0.83}Br_{0.17})₃ are synthesized utilizing a one-step solution process plus an anti-solvent wash technique and deployed in PVSCs with an inverted architecture. All films show a cubic crystal structure, demonstrating that compositional tuning of both the tolerance factor and crystallization rate allows for dense, single phase formation. The band gaps, affected by both lattice constriction and octahedral tilting, show opposite trends in Pb-rich or Sn-rich perovskites with the increase of Cs for fixed Sn compositions. The Cs_{0.05}(MA_{0.17}FA_{0.83})_{0.95}Pb_{0.25}Sn_{0.75}(I_{0.83}Br_{0.17})₃ PVSCs achieve a power conversion efficiency (PCE) of 11.05%, a record for any PVSC containing 75% Sn perovskites, and the Cs_{0.10}(MA_{0.17}FA_{0.83})_{0.90}Pb_{0.75}Sn_{0.25}(I_{0.83}Br_{0.17})₃ PVSCs reach a record PCE of 15.78%. Moreover, the triple cation and double halide alloyed Pb–Sn perovskites exhibit improved device stability under inert and ambient conditions. This study, which illustrates the impact of cation and halide tuning on alloyed Pb–Sn perovskites, can be used to further eliminate Pb and improve device performance of high Sn PVSCs and other optoelectronic devices.

Received 4th July 2018 Accepted 10th August 2018

DOI: 10.1039/c8ta06391e

rsc.li/materials-a

Introduction

Hybrid organic–inorganic lead halide perovskite solar cells (PVSCs) have emerged in the past decade as a promising low-cost thin film photovoltaic device with the power conversion efficiency (PCE) increasing from 3.8% to 22.7%.¹ The organic–inorganic perovskites have a formula of AMX₃, where A is a monovalent cation (*e.g.*, methylammonium (MA⁺, CH₃NH₃⁺), formamidinium (FA⁺, CH₃(NH₂)₂⁺), and/or cesium (Cs⁺)),² M is a divalent transition metal cation (*e.g.*, Pb²⁺ and/or Sn²⁺),³ and X is a halide anion (*e.g.*, I⁻, Br⁻, and/or Cl⁻).^{4,5} The intrinsic properties of perovskites, such as a high absorption coefficient over the visible spectrum,⁶ long carrier diffusion lengths,⁷ low exciton binding energy,⁸ high carrier mobility,⁹ and a direct band gap,¹⁰ have contributed to high device performance.

Pure lead perovskites come with instabilities that have hindered PVSC commercialization. Methylammonium based perovskites, such as MAPbI₃, have thermal instabilities that result in the degradation of methylammonium and a phase transition from the preferred black cubic α -phase to a noncentrosymmetric dark brown tetragonal β -phase at 55 °C.^{11,12}

Department of Chemical Engineering, University of Washington, Seattle, WA 98195, USA. E-mail: qyu@u.washington.edu

† Electronic supplementary information (ESI) available. See DOI: 10.1039/c8ta06391e

Due to the positive enthalpy of formation of MAPbI₃, it easily undergoes chemical reactions under ambient conditions and is degraded by water, oxygen, and light radiation, reverting the perovskite back to its precursors. 13,14 Although the cubic α-phase FAPbI₃ is thermally stable at high temperatures and can lead to more efficient solar cells, due to a lower band gap of 1.48 eV compared to that of 1.61 eV of MAPbI₃, it is still sensitive to humidity and undergoes a phase transition to a tetragonal β-phase at room temperature and also to a yellow photoinactive hexagonal δ-phase.¹² CsPbI₃ has been studied as an all-inorganic option for PVSCs to avoid the sensitivity to heat and humidity that is common in organic cation devices. Unfortunately, CsPbI₃ perovskites phase change from the favourable cubic α-phase to a yellow photoinactive hexagonal δ-phase at room temperature. This undesirable phase transition is due to the smaller radius of Cs⁺ (1.67 Å) being unable to support the PbI₆ octahedral frame necessary for a cubic crystal lattice. 15,16 Replacing I⁻ with the smaller Br⁻ has been shown to shrink this octahedral frame enough to stabilize the cubic α-phase, but this replacement tunes the band gap to 2.3 eV, making it unable to absorb long wavelength light, resulting in low PCE.¹⁷

To improve phase stability while also tuning the band gap, Snaith and co-workers partially replaced FA^+ with Cs^+ in mixed halide perovskites $FAPb(I_{1-z}Br_z)_3$, creating the cubic structure for all Br compositions tested with band gaps ranging from 1.48 to 2.3 eV. The $FA_{0.83}Cs_{0.17}Pb(I_{0.6}Br_{0.4})_3$ single junction solar cell

reached a maximum PCE of 17.1%.18 The high efficiencies for single-junction PVSCs have also been achieved by optimizing the compositions of the A- and X- sites of perovskites (such as $FA_{1-x}MA_xPb(I_{1-\nu}Br_{\nu})$). Grätzel and co-workers were able to consistently achieve >20% PCE for the PVSCs with the $(MA_{0.17}FA_{0.83})Pb(I_{0.83}Br_{0.17})_3$ perovskites. By mixing $(MAPbBr_3)_{0.17}$ with (FAPbI₃)_{0.83}, it can slow the crystallization process, creating smoother, reproducible films. The improved band alignment led to record short-circuit current densities. 19,20 Grätzel's group further introduced Cs to the A-site and demonstrated a device performance of 21.1% PCE with improved stability under ambient conditions for the $Cs_{0.05}(MA_{0.17}FA_{0.83})_{0.95} Pb(I_{0.83}Br_{0.17})_3$ PVSCs, which was attributed to the smaller Cs⁺ (1.67 Å) and MA⁺ (2.16 Å) ions "pushing" the larger FA⁺ (2.53 Å) ion into the black cubic α-phase.² Li and co-workers conducted a solvent engineering study using $Cs_{0.05}(MA_{0.17}FA_{0.83})_{0.95}Pb(I_{0.83}Br_{0.17})_3$ perovskites and reiterated the improved stability, performance, and reproducibility of the PVSCs by adding a small amount of Cs⁺.²¹ It is thus imperative to design mixed cation and halide perovskites to improve device stability.

To reduce the environmental toxicity of lead based PVSCs, tin was investigated as a replacement due to its similar electronic configuration to a group 14 metal and the ability to form a MX6 octahedron necessary for the cubic structure.22 The comparable ionic radius, Sn²⁺ (1.15 Å) and Pb²⁺ (1.19 Å), allows for minimized tolerance factor differences, optimizing cubic α phase stability.23 Sn-based perovskites also have the benefit of lower band gaps by forming Pb-Sn binary alloyed perovskites, such as MAPb_{0.3}Sn_{0.7}I₃, that reach the minimum band gap of 1.17 eV.24-26 Combining the transition metal tuning with the halide tuning has recently created an ideal band gap of 1.35 eV for MAPb_{0.5}Sn_{0.5}(I_{0.8}Br_{0.2})₃ perovskites that can lead to a theoretical Shockley-Queisser efficiency of 33%.²⁷ Unfortunately, the crystallization and stability of high Sn-containing perovskites have impeded the progress of Sn-based PVSCs. The reaction between MAI and SnI2 is recognized to be faster than that of PbI₂ due to the greater Lewis acidity of Sn²⁺ versus Pb²⁺, resulting in uncontrollable crystallization during solution processing.28 MASnI₃ perovskites are, therefore, prone to poor film coverage with micron sized pinholes limiting device performance without solvent or deposition engineering. Kanatzidis and co-workers obtained pinhole-free MASnI₃ perovskite films using N,N-dimethyl sulfoxide (DMSO) solvent to form a SnI2-·3DMSO complex intermediate phase. This intermediate phase allows the MA+ ions to react with SnI2 in a controlled manner where the rate-limiting step is the removal of DMSO through thermal annealing. The corresponding devices achieved a short circuit current density (I_{sc}) of 21.4 mA cm⁻².²⁹ Jen and coworkers developed a one-step solution thin film formation method using γ-butyrolactone (GBL): DMSO co-solvents to dissolve precursors combined with an anti-solvent toluene wash step to further control crystallization rates, which resulted in pinhole-free perovskite films and allowed for high performance of $MA_{0.5}FA_{0.5}Pb_{0.75}Sn_{0.25}I_3$ PVSCs reaching a PCE of 14.19%. 30 Sn-containing PVSCs have also been shown to degrade from the oxidation of Sn²⁺ to the more thermodynamically favoured Sn⁴⁺, even in inert atmospheres, due to the small formation energy

and relatively weak inert pair effects.28 The high levels of self-pdoping caused by Sn⁴⁺ limit the diffusion length for charge carriers. To reduce the oxidation of Sn2+, SnF2 was first added in the preparation of CsSnI₃ perovskite thin films to fill Sn vacancies with extra Sn²⁺ ions, suppressing Sn⁴⁺ centers as well as reducing Sn⁴⁺ back to a divalent metal.^{31,32} Attempts have since been made to utilize SnF2 as a reducing agent to improve the performance of high Sn PVSCs. Seok et al. used a pyrazine-SnF₂ complex to reduce Sn²⁺ oxidation and slow the crystallization of FASnI₃ perovskites and demonstrated a PCE of 4.8%.³³ Yan et al. later reported a record efficiency of 6.22% for FASnI₃ using SnF2 as a reducing agent on a p-i-n planar solar architecture.34 The introduction of Cs has also been shown to reduce the crystallization rate and improve the stability of compositions MAPb_{0.5}Sn_{0.5}I₃ and FAPb_{1-x}Sn_xI₃. Jen and co-workers showed that a 10% Cs addition improved the stability of MA_{0.9}Cs_{0.1}Pb_{0.5}Sn_{0.5}I₃ perovskites allowing for pristine, unencapsulated devices to retain 75% of the initial PCE after 12 days under inert conditions and 76% of the initial PCE after 20 days under ambient conditions.24

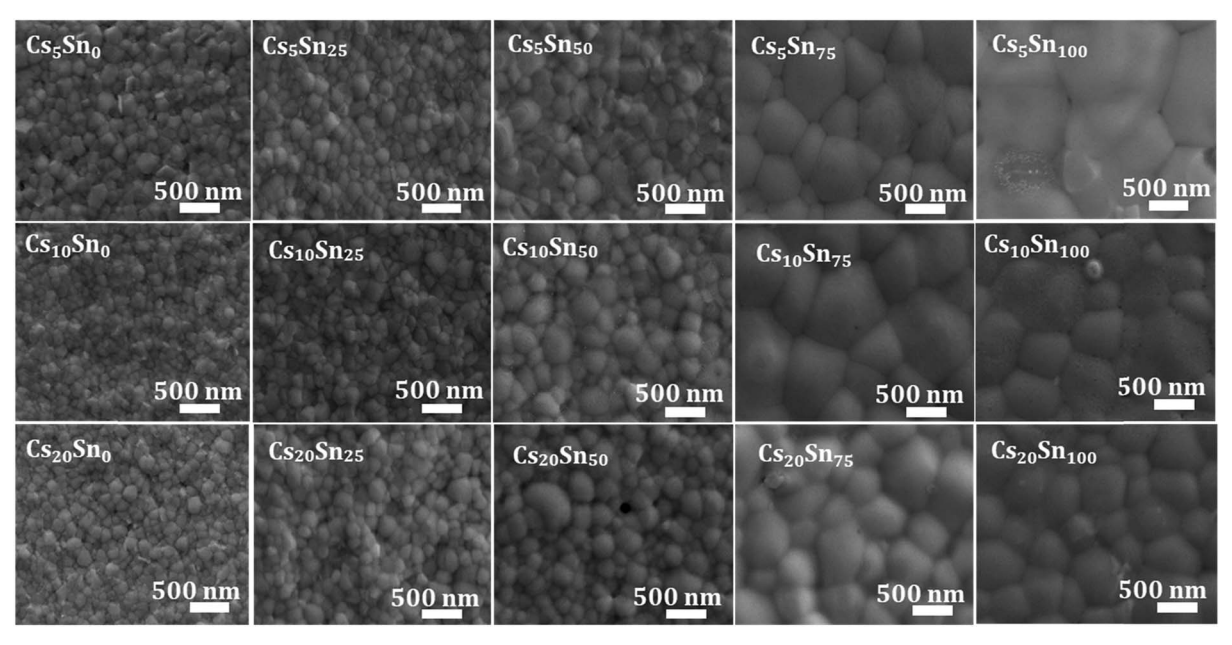
This gives rise to our strategy of using the triple Cs/MA/FA cation with mixed Br/I halide to stabilize high Sn PVSCs. In this work, we combined compositional tolerance factor tuning and solvent-washing methodology to create the first reproduction of cubic α-phase, homogeneous and densely packed polycrystalline $Cs_x(MA_{0.17}FA_{0.83})_{1-x}Pb_{1-y}Sn_y(I_{0.83}Br_{0.17})_3$ films with x = 0.05, 0.10, and 0.20 and y = 0, 0.25, 0.50, 0.75, and 1.0. Toimprove general device stability, we used a simple inverted device structure of indium tin oxide (ITO)/poly(3,4,-ethylenedioxythiophene): polystyrene sulfonate (PEDOT:PSS)/perovskite/[6,6]-phenyl-C₆₀-butyric acid methyl ester (PC₆₀BM)/ fullerene $(C_{60})/2$,9-dimethyl-4,7-diphenyl-1,10-phenanthroline (BCP)/Ag. This solar cell architecture eliminated the need for dopants that introduce instabilities and decreased hysteresis, allowing stable maximum power. Due to the high-quality film morphology and ideal single junction band gap (1.36 eV) of $Cs_{0.10}(MA_{0.17}FA_{0.83})_{0.9}Pb_{0.75}Sn_{0.25}(I_{0.83}Br_{0.17})_3,$ the PVSCs reached a maximum PCE of 15.78%. The triple cation mixture and SnF2 additive alleviated Sn oxidation for Cs0.05- $(MA_{0.17}FA_{0.83})_{0.95}Pb_{0.25}Sn_{0.75}(I_{0.83}Br_{0.17})_3$ (band gap = 1.30 eV), resulting in a record maximum PCE of 11.05% for the corresponding PVSC. Moreover, the 75% Sn PVSCs can retain 80% of the initial PCE after 30 days storage under inert conditions followed by over 100 hours under ambient conditions. The triple cation Pb-Sn double halide perovskites not only offer a wide tunability of the band gap to achieve ideal band gaps for single-junction or tandem PVSCs but also greatly improve the performance and stability of high Sn PVSCs, leading to the possibility of achieving stable, high efficiency lead-free devices.

Results and discussion

To achieve good film morphology, we used the one-step solution process and optimized anti-solvent engineering to synthesize dense, pinhole-free perovskite thin films. All precursors (MAI, FAI, PbI2, PbBr2, and FABr) were dissolved in a DMSO: GBL (3:7, v/v) co-solvent to a total concentration of 2.5 M. 10% mol SnF₂ with respect to the Sn content was added to suppress the formation of Sn⁴⁺. During spin coating, the anti-solvent wash with toluene was performed to remove excess DMSO from the complexes PbI₂·2DMSO and SnI₂·3DMSO to result in the rapid formation of A-PbI₂-DMSO and A-SnI₂-2DMSO intermediates. It has been previously shown that the PbI₂-DMSO composites yield an expanded lattice compared to neat PbI₂. This volume expansion facilitates the intramolecular exchange processing due to the volatility of the DMSO molecules in this adduct structure.35 One SnI2 forms a complex with 3 DMSO in the precursor solution due to the high bond energy of Sn-O (528 kJ mol⁻¹) compared to that of Pb-O (374 kJ mol⁻¹) supporting the preferential attachment of DMSO to Sn.36 In our previous work, we demonstrated the role of DMSO in enhancing MAPb_{1-x}Sn_xI₃ and MAPbCl₃ film morphology and crystallinity.^{37,38} The volume of toluene was decreased with increased Sn percentage and amount of complexes SnI₂·3DMSO to minimize multiple DMSO removal from the complexes before annealing. Multiple DMSO removal would create A-SnI2-DMSO instead of A-SnI2-2DMSO intermediates, hindering the slower controlled removal of DMSO and reaction upon annealing, resulting in pinholes. All the films, except those of 100% Sn, were annealed at 100 °C for 10 min to remove complexed DMSO under a controlled reaction of the metal and cation during the annealing step, creating homogeneous, densely packed Pb-Sn perovskite films with clear grain boundaries. Films with 10 and 20% Cs and pure Sn were found to have better morphology when annealed at 110 °C, most likely due to the stronger bond in the A-SnI₂-2DMSO complex, which would require a higher temperature to break.

Fig. 1 shows the scanning electron microscopy (SEM) images of the perovskite thin films with the compositions of $Cs_x(MA_{0.17}FA_{0.83})_{1-x}Pb_{1-y}Sn_y(I_{0.83}Br_{0.17})_3$, where x = 0.05, 0.1, and 0.2 and y = 0, 0.25, 0.50, 0.75, and 1.0. The low magnification SEM images are shown in Fig. S1† to demonstrate the film quality and quantify the average grain sizes. To make the description simple, we will use the notation Cs_xSn_y to represent the thin films. For example, Cs₅Sn₂₅ represents thin films with the composition of Cs_{0.05}(MA_{0.17}FA_{0.83})_{0.95}- $Pb_{0.75}Sn_{0.25}(I_{0.83}Br_{0.17})_3$. As shown in Fig. 1, for each Cs composition, the grain size increased slightly with the addition of Sn to 50%. A notable grain size increase was observed when the Sn composition was greater than 50%. This could be due to the higher coordination of DMSO to Sn (A-SnI₂-2DMSO) compared to Pb (A-PbI2-DMSO) formed for high Sn composition intermediates, allowing for even slower crystallization upon annealing as one mole of DMSO is first removed (A-SnI₂-DMSO) followed by the second, thus leading to larger grains. Sn addition has been shown to increase grain size with large grains for high Sn perovskites. 32 For each Sn composition, Cs addition had no notable changes in grain size. The large area SEM images (Fig. S1†) shows that pinhole-free films were formed for all Cs compositions with 50% Sn or lower. Smooth, dense, pinhole-free morphologies were also formed for the Cs₅Sn₇₅ and Cs₁₀Sn₇₅ films while obvious pinholes were formed in the Cs₂₀Sn₇₅ film. The Cs₅Sn₁₀₀ film has the largest, most prominent pinholes as well as an amorphous phase around the grain boundaries with a poor morphology apparent in Fig. S1† while both Cs₁₀Sn₁₀₀ and Cs₂₀Sn₁₀₀ films have a few, small pinholes and more even coverage. A few smaller, lighter grains appeared in the Cs₁₀Sn₁₀₀ and Cs₂₀Sn₁₀₀ films, which could be due to a slight phase segregation.

The thin films were further characterized with X-ray diffraction (XRD) to determine the phase and crystallinity. As shown in Fig. 2a, all thin films have a cubic α-phase with the $Pm\bar{3}m$ space group. The absence of additional peaks, such as the photoinactive hexagonal δ-phase FAPbI₃ at 11.63°, the orthorhombic δ-phase CsPbI₃ at 9.80° and 13.00°, the unreacted, cubic PbI2 at 12.85°, and the tetragonal perovskite peaks



 $\textbf{Fig. 1} \quad \text{SEM images of } \textbf{Cs}_{x} (\textbf{MA}_{0.17} \textbf{FA}_{0.83})_{1-x} \textbf{Pb}_{1-y} \textbf{Sn}_{y} (\textbf{I}_{0.83} \textbf{Br}_{0.17})_{3} \text{ perovskite thin films with } \\ x = 0.05, \, 0.1 \text{ and } 0.2 \text{ and } y = 0, \, 0.25, \, 0.50, \, 0.75 \text{ and } 1.0.0 \text{ and } 1.0.0$

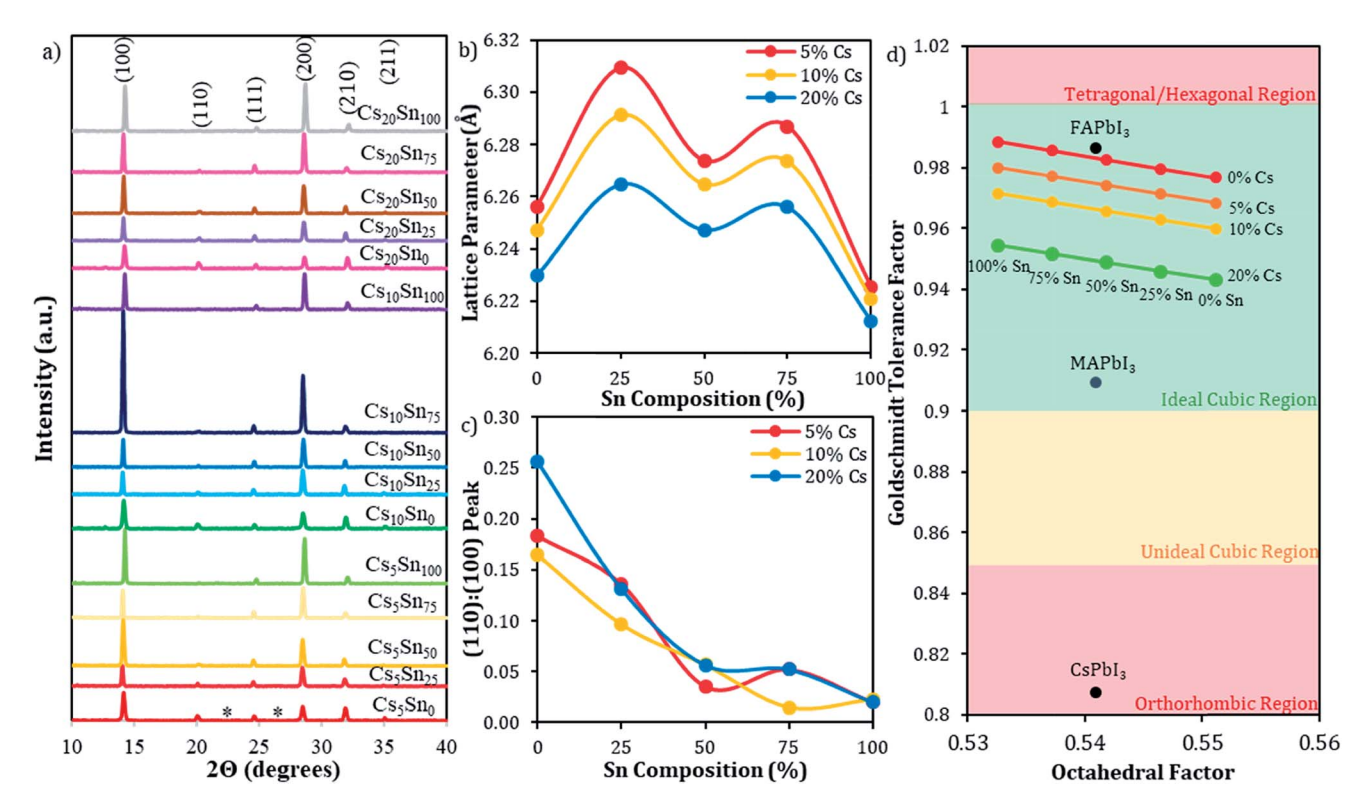


Fig. 2 (a) X-ray diffraction (XRD) patterns of $Cs_x(MA_{0.17}FA_{0.83})_{1-x}Pb_{1-y}Sn_y(I_{0.83}Br_{0.17})_3$ perovskite thin films with x=0.05, 0.1 and 0.2 and y=0, 0.25, 0.50, 0.75 and 1.0. (b) The cubic lattice parameters as a function of Sn composition for each Cs composition of all perovskites. (c) The intensity ratio of the (110) and (100) peaks $(I_{(110)}/I_{(100)})$ as a function of Sn composition for each Cs composition of all perovskites. (d) The Goldschmidt tolerance and octahedral factor calculations for corresponding compositions with phase change regions.

indicated by the asterisk symbol confirms the pure crystalline phase of the synthesized perovskite films.34,39,40 The strong diffraction from the (100) and (200) planes indicates a favourable orientation with the glass substrate. The shifts of the (100) diffraction peak for all synthesized perovskite films are clearly shown in Fig. S2.† For increasing Cs with a fixed Sn, the (100) peak right shifts (Fig. S2a†), resulting in a reduced lattice parameter (Fig. 2b) because of the incorporation of the smaller Cs ion (r = 1.67 Å), supporting the successful incorporation of Cs.41,42 Fig. 2d illustrates that the incorporation of the smaller Cs ion pushes the Goldschmidt tolerance factor into a more cubic region for all Sn compositions and further from the hexagonal region, which stabilizes the perovskites against unwanted phase changes. The addition of Cs was also used to further optimize the Goldschmidt tolerance factor (GTF) of the perovskite compositions. The GTF was first used for metal-oxide perovskites and has been applied to metal-halide perovskites as a way to quasi-quantify the stability of various composition perovskites. 15,43 The GTF of a 3D cubic ABX3 perovskite is represented by:

$$GTF = \frac{(r_A + r_X)}{\sqrt{2}(r_B + r_X)}$$

where r_A , r_B and r_X are the ionic radii of the monovalent cation, divalent transition metal cation, and halide anion, respectively. The radii of MA⁺ (2.16 Å), FA⁺ (2.53 Å), Cs⁺ (1.67 Å), Pb²⁺ (1.19 Å), Sn^{2+} (1.15 Å), I^{-} (2.20 Å), and Br (1.96 Å) were used to calculate

the GTFs of all perovskites. 44 The octahedral factor (μ) is another quantifying ratio of divalent transitional metal cation radium to halide anion radium (r_B/r_X) . Stable cubic α -phase perovskites are expected to exhibit a GTF between 0.8 and 1 and an octahedral factor, μ , between 0.44 and 0.90.45 Experimentally, perovskites are more stable when the GTF is between 0.9 and 1 as GTFs > 1 result in the hexagonal/tetragonal phase and GTFs < 0.8 result in the orthorhombic phase. The GTFs and octahedral factors of $Cs_x(MA_{0.17}FA_{0.83})_{1-x}Pb_{1-y}Sn_y(I_{0.83}Br_{0.17})_3$ perovskites with x = 0, 0.05, 0.1 and 0.2 and y = 0, 0.25, 0.5, 0.75 and 1 are graphed in Fig. 2d. In addition, these factors of CsPbI₃, MAPbI₃ and FAPbI₃ are also marked in the graph. As shown in Fig. 2d, all perovskites tested fall in the cubic phase range of the octahedral factor. The GTF is shown to increase with the increasing of Sn composition and decreases with the increasing of Cs composition. MAPbI3 and FAPbI3 are at the lower and higher boundary of the GTF region for the ideal cubic phase, respectively. Even though the tolerance factor of α-FAPbI₃ is 0.986 calculated based on the radium of FA⁺ (2.53 Å), the non-sphericity of FA⁺ complicates the calculation, resulting in an actual tolerance factor around 1.03.46 This tolerance factor borders in the hexagonal region (GTF > 1) at room temperature, explaining the instabilities of α-FAPbI₃. Adding MA and Br to form $(MA_{0.17}FA_{0.83})Pb(I_{0.83}Br_{0.17})_3$ (i.e., Cs_0Sn_0) allows for a smaller tolerance factor (0.977) moving more into the cubic phase region. However, forming Pb-Sn alloy perovskites based on this mixed MA/FA and I/Br formula leads to increased GTFs

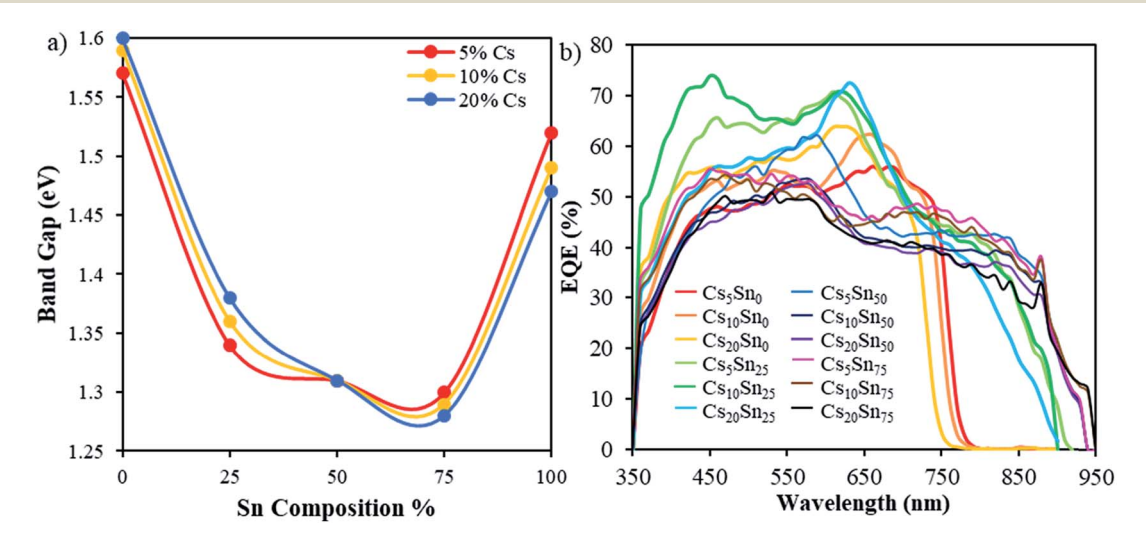
with increasing Sn contents. Cs₀Sn₁₀₀ reaches a GTF of 0.989, exceeding that of FAPbI3. Introducing Cs can decrease GTFs, allowing for even pure Sn perovskites to have a more cubic tolerance. For example, adding 5, 10 and 20% Cs, i.e., Cs₅Sn₁₀₀, $Cs_{10}Sn_{100}$ and $Cs_{20}Sn_{100}$, decreases the GTFs to 0.980, 0.972 and 0.954, respectively. The lower GTFs indicate that introducing Cs can entropically stabilize the perovskites at room temperature, likely leading to higher stabilities. This is in good agreement with previous reports of triple cation mixtures for tolerance tuning.15,41,47 Using the three-cation mixture also alleviates the size mismatch of Cs and FA, decreasing the chance of entropic phase separation.

While the lattice parameters decreased slightly from pure Pb to pure Sn for all fixed Cs compositions, all Pb-Sn alloys exhibited larger lattice parameters than the pure Pb or Sn perovskites with dips at 50% Sn (Fig. 2b). This nonlinear deviation is consistent for all Cs compositions. McGehee and co-workers reported slight nonlinear deviations of lattice parameters for $Cs_vFA_{1-v}Pb_xSn_{1-x}I_3$ perovskites. This could be due to the nonlinear Pb-X-Sn bond which resulted from octahedral tilting which creates a nonlinear lattice effect for Pb-Sn alloyed perovskites during the incorporation of more Sn. However, the trends are different. For example, our CsxSn25 perovskites have larger lattice parameters than those of Cs_xSn₀ perovskites while the lattice parameter of the FAPb_{0.75}Sn_{0.25}I₃ perovskite is smaller than that of the FAPbI₃ perovskite.⁴⁸ The opposite trend could be attributed to the smaller lattice parameters of Cs_rSn₀ in the range of 6.26-6.23 Å (Fig. 2b) compared to $Cs_{\nu}FA_{1-\nu}Pb_{0.75}Sn_{0.25}I_3$ in the range of 6.39–6.33 Å due to the introduction of the smaller MA⁺ and Br⁻. The smaller overall lattice parameter in our perovskites could make the octahedral tilting resulted nonlinearity of the mixed Pb-X-Sn bond more prominent, allowing certain Pb-Sn alloyed perovskites to have a larger lattice parameter than pure Pb or Sn perovskites.

In addition, it was noticed that the full width at half maximum (FWHM) of the (100) peak becomes narrower with Sn

addition when compared to the pure Pb perovskites (Fig. S2†), indicating the high crystallinity of the 25-75% Sn perovskites, which is consistent with the grain growth shown in the SEM images in Fig. 1. Fig. 2c shows the intensity ratio of the (110) and (100) peaks for all compositions of perovskites, illustrating the decrease in (110) peak intensity with addition of Sn. For 75% and 100% Sn compositions, there is a significant decrease in the (110) and (111) peaks showing a more preferred orientation of the (100) plane.

The **UV-Vis** absorption spectra the $Cs_x(MA_{0.17}FA_{0.83})_{1-x}Pb_{1-y}Sn_y(I_{0.83}Br_{0.17})_3$ perovskite thin films are shown in Fig. S3a-c.† As the incorporation of Sn was increased to 100%, the absorption spectra showed a softened band edge due to sub-band gap states and scattering, making it difficult to determine the band gap. Photoluminescence (PL) measurements were, therefore, performed with samples sealed in a vacuum to better define the band gap trend (Fig. S3d†). The band gaps estimated from the onsets of the absorption spectra (0-75% Sn compositions) and PL spectra (100% Sn composition) are graphed as a function of Sn composition for different Cs contents (Fig. 3a). For each fixed Cs composition, the band gaps decrease from the maxima around 1.57-1.61 eV of the pure Pb perovskites to the minima around 1.28-1.30 eV of the perovskites with 75% Sn and then increase to 1.47-1.52 eV for 100% Sn. The addition of Cs, however, causes two trends in the band gap depending on the Sn composition and the cross-over occurs at 50% Sn. The band gaps increase with the increase of Cs for Pb-rich perovskites while they decrease with the increase of Cs for Sn-rich perovskites. All these trends are mainly due to the influence of the M-X overlap and the A-site induced MX₆ octahedral tilting on the conduction and valence band edges of perovskites. First-principles electronic structure calculations have determined that the conduction band minimum of metal halide perovskites is a hybrid of metal p and halide p orbitals with nonbonding character and the valence band maximum is an antibonding hybrid of metal s and halide p orbitals.49 Changes in the M-X overlap, therefore, raise the energy of the



 $Fig. \ 3 \quad \text{(a) The band gap of } Cs_x (MA_{0.17}FA_{0.83})_{1-x}Pb_{1-y}Sn_y (I_{0.83}Br_{0.17})_3 \ \ perovskite \ thin \ films \ as \ a \ function \ of \ Sn \ composition \ for \ different \ Cs_{0.83}(MA_{0.17}FA_{0.83})_{1-x}Pb_{1-y}Sn_y (I_{0.83}Br_{0.17})_3 \ \ perovskite \ thin \ films \ as \ a \ function \ of \ Sn \ composition \ for \ different \ Cs_{0.83}(MA_{0.17}FA_{0.83})_{1-x}Pb_{1-y}Sn_y (I_{0.83}Br_{0.17})_3 \ \ perovskite \ thin \ films \ as \ a \ function \ of \ Sn \ composition \ for \ different \ Cs_{0.83}(MA_{0.17}FA_{0.83})_{1-x}Pb_{1-y}Sn_y (I_{0.83}Br_{0.17})_3 \ \ perovskite \ thin \ films \ as \ a \ function \ of \ Sn \ composition \ for \ different \ Cs_{0.83}(MA_{0.17}FA_{0.83})_{1-x}Pb_{1-y}Sn_y (I_{0.83}Br_{0.17})_3 \ \ perovskite \ thin \ films \ as \ a \ function \ of \ Sn \ composition \ for \ different \ Cs_{0.83}(MA_{0.17}FA_{0.83})_{1-x}Pb_{1-y}Sn_y (I_{0.83}Br_{0.17})_3 \ \ perovskite \ thin \ films \ as \ a \ function \ for \ different \ Cs_{0.83}(MA_{0.17}FA_{0.83})_{1-x}Pb_{1-y}Sn_y (I_{0.83}Br_{0.17})_3 \ \ perovskite \ thin \ films \ as \ a \ function \ for \ different \ Cs_{0.83}(MA_{0.17}FA_{0.83})_{1-x}Pb_{1-y}Sn_y (I_{0.83}Br_{0.17})_3 \ \ perovskite \ for \ Cs_{0.83}(MA_{0.17}FA_{0.83})_{1-x}Pb_{1-y}Sn_y (I_{0.83}Br_{0.17})_3 \ \ perovskite \ films_{0.83}(MA_{0.17}FA_{0.83})_{1-x}Pb_{1-y}Sn_y (I_{0.83}Br_{0.17})_3 \ \ perovskite \ films_{0.83}(MA_{0.17}FA_{0.83})_{1-x}Pb_{1-y}Sn_y (I_{0.83}Br_{0.17})_3 \ \ perovskite_{0.83}(MA_{0.17}FA_{0.83})_3 \ \ perovskite_{0.83}(MA_{0.17}FA_{0.83})$ contents. (b) The EQE spectra of PVSCs with the $Cs_x(MA_{0.17}FA_{0.83})_{1-x}Pb_{1-y}Sn_y(I_{0.83}Br_{0.17})_3$ active layers

valence band more directly while the conduction band, having less orbital overlap, responds less strongly to lattice distortions, allowing the band gap to decrease with increased M-X overlap. Although the Sn-X-Sn bond increases the orbital overlap compared to the Pb-X-Pb bond, the mixed Pb-X-Sn bonds allow for spin-orbital coupling and the least distorted, more linear Pb-X-Sn bond angles, resulting in the minimum band gaps at 75% Sn. The minimum band gaps at 75% Sn observed in this work for triple cation, double halide Pb-Sn perovskites follow the same trend for single cation, single halide MAPbx-Sn_{1-x}I₃ perovskites.²⁶ The opposite trend of band gap change with Sn composition was also observed in FA_{1-x}Cs_xPb_{1-v}Sn_vI₃ perovskites, where x ranged from 0 to 30% and y ranged from 0 to 100%.48 A smaller A-site cation could increase the MX6 octahedra tilting, which would increase the band gap or contract the crystal lattice isotropically, which would decrease the band gap.48 The pure Pb and Pb-rich perovskites show a blue shift in the band gap with increased Cs in the A-site, which is predominantly due to the MX6 tilting decreasing the M-X overlap, lowering the valence band. The pure Sn and Sn-rich perovskites follow the opposite trend, a red shift in the band gap with increased Cs in the A-site, which is mainly due to the isotropical lattice constrictions, resulting in an increasing M-X overlap. 48,50 Our results support these two mechanisms for Asite induced band gap changes in previous literature while also showing the shift in predominant mechanisms occurring at 50% Sn even for triple cation, double halide Pb-Sn perovskites.

band trends of $Cs_x(MA_{0.17}FA_{0.83})_{1-x}$ $Pb_{1-\nu}Sn_{\nu}(I_{0.83}Br_{0.17})_3$ perovskites determined from UV-Vis and PL spectra were also shown in the external quantum efficiency (EQE) spectra of PVSCs made with these films. As shown in Fig. 3b, fixed Cs with increasing Sn results in a red shift in EQE edges from 0-75% Sn. With fixed Sn and increasing Cs, there is a blue shift in the EQE edge for Sn₀ and Sn₂₅ and no change for Sn_{50} , while there is a red shift for Sn_{75} .

To determine the viability of these films as solar cell active layers, PVSCs were fabricated using $Cs_x(MA_{0.17}FA_{0.83})_{1-x}Pb_{1-y}Sn_y$ $(I_{0.83}Br_{0.17})_3$ as the active layer with the inverted perovskite architecture of ITO/PEDOT:PSS/perovskite/PC60BM/C60/BCP/Ag as shown in the cross-sectional SEM image in Fig. 4a. PEDOT:PSS acts as the solution processable hole transport layer (HTL) sandwiching the perovskite layer with the spin-coated electron transport layer (ETL) PC₆₀BM, which is commonly used to fill gaps in the perovskite layer, reducing surface roughness and passivating possible traps.51 The thermally deposited C60 layer acts as a second ETL to improve band energy alignment and the BCP layer acts as a hole blocking layer (HBL) to increase charge separation and minimize recombination. Although the common device architecture for Sn-based PVSCs has the configuration of mesoporous TiO₂/perovskite/spiro-OMeTAD/ Au, the spiro-OMeTAD HTL uses dopants such as lithium bis(trifluoromethylsulfonyl)imide salt and 4-tert-butylpyridine to better align the spiro-OMeTAD work function with the active layer, facilitating hole extraction. These dopants have been shown to be reactive and introduce further instability into Snbased perovskites under inert conditions.6 The use of mesoporous TiO2 as an ETL also requires a high sintering

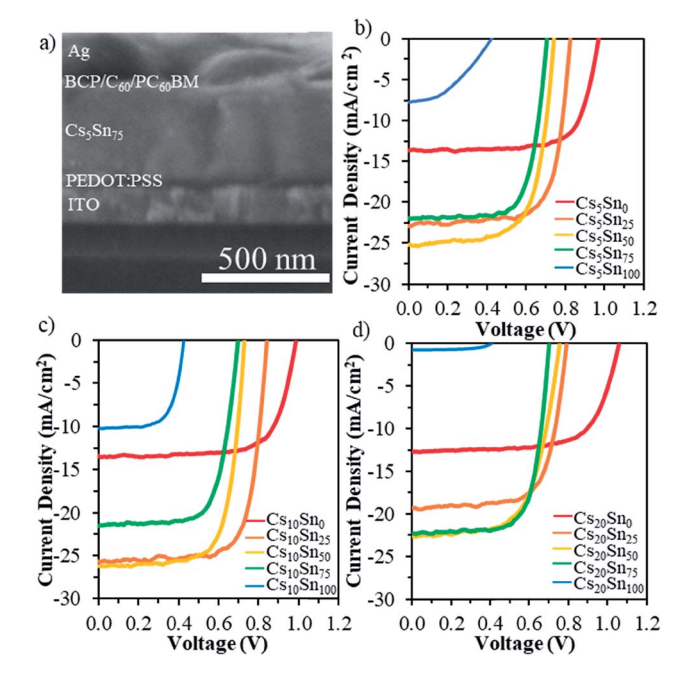


Fig. 4 (a) Cross-sectional SEM image showing the $Cs_{0.05}(MA_{0.17} FA_{0.83}$)_{0.95}Pb_{0.25}Sn_{0.75} ($I_{0.83}Br_{0.17}$)₃ PVSC with the following layers: ITO \sim 200 nm)/PEDOT:PSS (\sim 50 nm)/perovskite (\sim 450 nm)/PC₆₀BM/C₆₀ (20 nm)/BCP (8 nm)/Ag (150 nm). The current density-voltage (J-V)characteristics of $Cs_x(MA_{0.17}FA_{0.83})_{1-x}Pb_{1-y}Sn_y(I_{0.83}Br_{0.17})_3$ PVSCs with (b) x = 0.05, (c) x = 0.10, and (d) x = 0.20 with y = 0, 0.25, 0.50, 0.75, and 1.0 for each x under AM 1.5 illumination at a scan rate of $0.01 \,\mathrm{V \, s^{-1}}$ from 0 to 1.2 V.

temperature, which is not ideal for mass manufacturing. The low temperature fabrication of the inverted structural PVSCs allows for adaptation to roll-to-roll processing, lowering manufacturing costs, improving intrinsic device stability, and lowering current density-voltage (I-V) hysteresis. 52

The photocurrent density-voltage (J-V) characteristics of the fabricated PVSCs are shown in Fig. 4b-d with detailed photovoltaic parameters summarized in Table 1. To determine the effects of Sn additives, pure Pb PVSCs were fabricated as a control for the three Cs compositions. The open-circuit voltage (V_{oc}) , short-circuit current density (J_{sc}) , fill factor (FF) and PCE as a function of Sn composition for different Cs contents are plotted in Fig. S4a-d,† respectively. The average $V_{\rm oc}$ s decrease from \sim 1.0 V to \sim 0.4 V with increase in Sn from 0 to 100% for all three Cs contents, which has been previously attributed to mismatched energy levels from valence decrease in band gaps from 1.57-1.61 to \sim 1.32 eV (Fig. 3a). The smaller band gaps allow for an increased photo-response in the near infrared region as demonstrated in the EQE spectra in Fig. 3b. On further increasing Sn to 75 and 100%, different Cs content PVSCs exhibited different trends. The J_{sc} of Cs₅Sn₇₅ was maintained at around 21 mA cm⁻² because of both a low band gap (\sim 1.3 eV) (Fig. 3a) and high-quality film (Fig. S1†). For Cs₅Sn₁₀₀, the $J_{\rm sc}$ decreased to 5.67 mA cm⁻² due to the introduction of large pinholes plus decreased crystallinity of the Cs₅Sn₁₀₀ perovskite film shown in Fig. S1.† For $Cs_{20}Sn_{75}$, the J_{sc} was decreased slightly to the still reasonable level of 20 mA cm⁻²

Table 1 Photovoltaic parameters of $Cs_x(MA_{0.17}FA_{0.83})_{1-x}Pb_{1-y}Sn_y(I_{0.83}Br_{0.17})_3$ PVSCs measured under AM 1.5 illumination obtained from forward J-V measurements

Device	$V_{\rm oc}$ (V)	$J_{\rm sc}~({ m mA~cm}^{-2})$	FF	PCE (%)	PCE_{max}
Cs_5Sn_0	0.98 ± 0.01	12.55 ± 1.03	0.70 ± 0.03	8.61 ± 0.75	9.54
Cs_5Sn_{25}	0.82 ± 0	20.98 ± 1.35	0.71 ± 0.01	12.29 ± 0.52	13.45
Cs_5Sn_{50}	0.73 ± 0.01	21.60 ± 2.09	0.67 ± 0.01	10.66 ± 1.19	12.71
Cs_5Sn_{75}	0.71 ± 0.01	21.46 ± 0.57	0.71 ± 0.01	10.81 ± 0.15	11.05
Cs_5Sn_{100}	0.43 ± 0.01	5.67 ± 2.97	0.52 ± 0.07	1.30 ± 0.80	1.87
$Cs_{10}Sn_0$	0.98 ± 0.01	12.37 ± 0.76	0.69 ± 0.03	8.46 ± 0.79	9.56
$Cs_{10}Sn_{25}$	0.83 ± 0.01	22.39 ± 2.62	0.73 ± 0.01	13.54 ± 1.74	15.78
$Cs_{10}Sn_{50}$	0.72 ± 0.01	23.14 ± 2.69	0.65 ± 0.08	10.91 ± 2.60	13.52
$Cs_{10}Sn_{75}$	0.68 ± 0.02	20.19 ± 1.92	0.66 ± 0.04	9.01 ± 1.01	10.45
$Cs_{10}Sn_{100}$	0.41 ± 0.00	8.98 ± 1.39	0.65 ± 0.02	2.43 ± 0.45	2.81
$Cs_{20}Sn_0$	1.04 ± 0.03	11.85 ± 0.92	0.64 ± 0.04	7.92 ± 1.29	9.23
$Cs_{20}Sn_{25}$	0.78 ± 0.01	17.50 ± 1.16	0.69 ± 0.01	9.36 ± 0.60	10.56
$Cs_{20}Sn_{50}$	0.75 ± 0.01	22.07 ± 1.50	0.61 ± 0.04	9.99 ± 0.66	10.81
$Cs_{20}Sn_{75}$	0.70 ± 0.01	20.74 ± 1.19	0.67 ± 0.07	9.77 ± 1.31	11.01
Cs ₂₀ Sn ₁₀₀	0.39 ± 0.03	1.34 ± 0.04	0.41 ± 0.05	0.21 ± 0.04	0.25

most likely due to the introduction of small numbers of pinholes (Fig. S1†). A significant decrease of J_{sc} to 8.98 mA cm⁻² was observed for Cs₁₀Sn₁₀₀, which could be due to the band gap increase (~1.44 eV) (Fig. 3a) and the small particles around grain boundaries resulted from phase segregations (Fig. S1†). The overall improvement in J_{sc} demonstrates the beneficial role of Cs in improving crystallinity and film formation. The $C_{20}Sn_{100}$ PVSCs exhibited the lowest J_{sc} of 1.34 mA cm⁻², indicating the necessity for specified Cs tuning to optimize film formation and Isc. Regardless of the Cs content, the FFs showed minimal variations for different Sn compositions. Combined with all parameters, the Cs₁₀Sn_v PVSCs have the highest maximum PCE for each Sn composition. The Cs₁₀Sn₂₅ and Cs₅Sn₇₅ PVSCs currently hold the record high maximum PCEs, 15.78 and 11.05%, respectively, for all reported PVSCs with 25 and 75% Sn compositions and architectures. The PVSCs with 75% Sn and all three Cs contents (Cs₅Sn₇₅, Cs₁₀Sn₇₅ and Cs₂₀Sn₇₅) exhibited the maximum PCE of 11.05, 10.45, and 11.01%, respectively, all surpassing the record PCE for 75% Sn $(7.8\% \text{ with } FA_{0.8}Cs_{0.2}Sn_{0.75}Pb_{0.25}I_3)^{53}$ and nearby 80% Sn $(7.07\% Cs_{0.2}Sn_{0.75}Pb_{0.25}I_3)^{53}$ with MAPb_{0.2}Sn_{0.8}I₃).⁵⁶ This could be due to the higher V_{oc} with the $V_{\rm oc}$ averages of 0.71, 0.68 and 0.70 V for Cs_5Sn_{75} , $Cs_{10}Sn_{75}$ and Cs20Sn75, respectively, demonstrating that composition tuning through triple cation and double halide mixtures might improve band energy alignment in the inverted architecture. Although Grätzel and co-workers demonstrated a higher PCE for the respective $Cs_{0.05}(MA_{0.17}FA_{0.83})_{0.95}Pb(I_{0.83}Br_{0.17})_3$ (Cs₅Sn₀) and $Cs_{0.1}(MA_{0.17}FA_{0.83})_{0.9}Pb(I_{0.83}Br_{0.17})_3$ ($Cs_{10}Sn_0$) devices, the TiO_2 solar architecture allows for a higher average V_{oc} of 1.13 V as well as an improved FF and Jsc.2 Liang and co-workers reported a similar inverted PEDOT:PSS architecture and toluene anti-solvent wash method resulting in photovoltaic parameters for the maximum forward scan of Cs₁₀(MA_{0.17}FA_{0.83})₉₀- $Pb(I_{0.83}Br_{0.17})_3$ devices (PCE = 9.51%, $V_{oc} = 0.94 \text{ V}$, FF = 0.53, J_{sc} = 16.95 mA cm $^{-2}$), which are comparable to our best performance $Cs_{10}Sn_0$ device (PCE = 9.56%, V_{oc} = 0.99 V, FF = 0.72, J_{sc} = 13.42 mA cm⁻²), demonstrating the reproducibility of the anti-solvent wash method for our controls as we fabricated new

compositions with Sn. It is worth noting that further PCE improvements of all high and pure Sn PVSCs can be achieved with further film optimization to remove pinholes and increase phase purity and crystallinity.

The hysteresis in J-V characteristics has been previously observed in PVSCs and has been attributed to a number of factors such as slow dynamic processing from trapping and detrapping of charge carriers, ferroelectric properties of perovskites, and ion migration.54,55 To determine the intrinsic hysteresis and device stability, forward/backward J-V scans and measurements of photocurrent stability at the maximum power were performed. As shown in Fig. 5a-c, forward and backward scans exhibited negligible hysteresis for almost all Sn and Cs composition PVSCs. The pure Pb compositions had complete overlap for the forward and backward scans for 5% and 10% Cs. 25% and 50% Sn also had stable scans except for 20% Cs. The noticeable hysteresis in Cs₂₀Sn₇₅ could be attributed to the small pinholes introduced into the film morphology, which could increase trapping of charge carriers. As shown in the photocurrent versus time measurements at the maximum power in Fig. 5d, the Cs_xSn₂₅ PVSCs, which had the highest performance parameters, remained stable under illumination in an inert atmosphere within a 30 min test period.

A critical issue for Sn-based PVSCs is the ambient environment instability caused by the oxidation of $\rm Sn^{2+}$ to $\rm Sn^{4+}$ and degradation in humidity. To understand the effects of the various Cs compositions on the stability of Pb–Sn PVSCs, the long-term device stability under inert and ambient conditions were evaluated. Fig. S5 and S6† show the device performance of PVSCs over 30 days under inert conditions (glove box, $\rm O_2 < 10$ ppm, $\rm H_2O < 10$ ppm) and after an additional 5 days under ambient conditions, respectively. Fig. 6 characterizes the normalized $V_{\rm oc}$, $J_{\rm sc}$, FF and PCE for PVSCs as a function of Sn composition for each Cs content at the 30th day under inert and the 5th day under ambient conditions following storage in the glove box for 30 days, comparing them to pristine devices. The 100% Sn PVSCs were omitted from stability tests due to their low performance under pristine conditions while the pure Pb

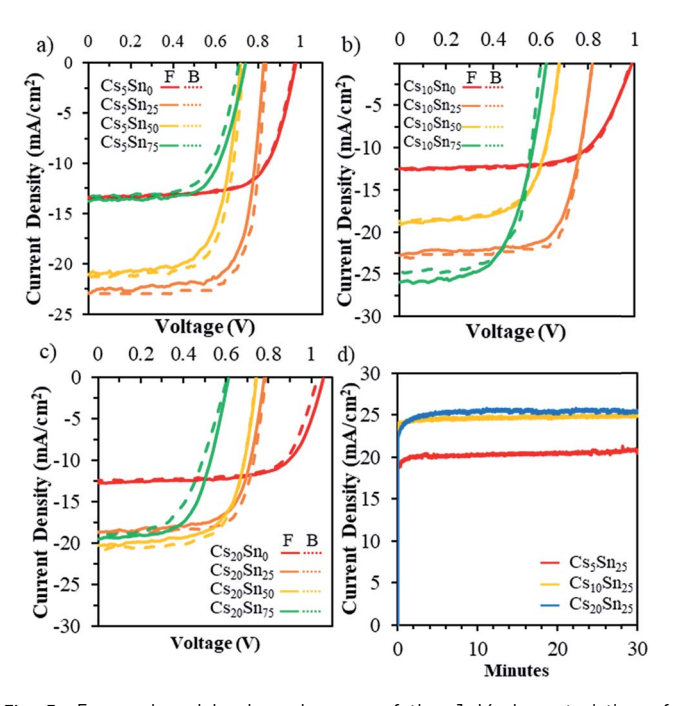


Fig. 5 Forward and backward scans of the J-V characteristics of $\mathsf{Cs_x}(\mathsf{MA_{0.17}FA_{0.83}})_{1-x}\mathsf{Pb_{1-y}Sn_y}(\mathsf{I_{0.83}Br_{0.17}})_3 \ \ \mathsf{PVSCs} \ \ \mathsf{at} \ \ \mathsf{a} \ \ \mathsf{scan} \ \ \mathsf{rate} \ \ \mathsf{of}$ 0.01 V s⁻¹ under AM 1.5 illumination: (a) x = 0.05, (b) x = 0.10, and (c) x = 0.20 with y = 0, 0.25, 0.50, 0.75, and 1.0 for each x. F indicates the forward scan from 0 to 1.2 V and B indicates the backward scan from 1.2 to 0 V. (d) The steady-state photocurrent measurements for $Cs_x(MA_{0.17}FA_{0.83})_{1-x}Pb_{0.75}Sn_{0.25}(I_{0.83}Br_{0.17})_3$ PVSCs with x = 0.05, 0.10,and 0.20.

PVSCs were omitted from the air exposure measurements due to their already degraded state after 30 days in the glove box. The $V_{\rm oc}$ of all PVSCs tested retained at least 87% of their original values under inert and ambient conditions demonstrating the stability of band energy alignments. Although there is fluctuation in FF values with air exposure, the biggest contributor to PCE degradation is the J_{sc} , which can be attributed to the SnF₂ segregation. Although the XRD (Fig. S7†) and SEM images (Fig. S8†) were taken from the perovskite films that were air exposed for 10 days, which may have exacerbated the segregation/degradation process, there could still be some ion migration in the active layers of the PVSCs under inert conditions that affected the J_{sc} over 30 days. Sn containing PVSCs stored under inert conditions all maintained 80% of the original PCE. The Cs_5Sn_{75} , Cs_5Sn_{50} , $Cs_{10}Sn_{50}$, $Cs_{20}Sn_{25}$, and $Cs_{20}Sn_{50}$ PVSCs all had an increase in PCE over time and finished the 30 days period with a normalized PCE at 1 or higher. We proposed that the SnF₂ enhanced phase segregation created highly conductive Sn, F, and Br rich particles as shown in the energy dispersive spectroscopy (EDS) measurements (Fig. S9 and Table S1†), temporarily increasing the J_{sc} before further segregation resulting in more recombination centers. All the devices were moved out of the glove box after 30 days and stored under ambient conditions and tested. After leaving under ambient conditions with 35 \pm 5% humidity for 5 days, the Cs₅Sn₅₀, Cs₁₀Sn₅₀, Cs₁₀Sn₇₅ and Cs₂₀Sn₇₅ PVSCs can retain over 80% of the original PCE. The Cs₅Sn₅₀ and Cs₂₀Sn₇₅ PVSC retained 90 and 92% of the original PCEs, respectively, demonstrating that Cs can be used to improve the stability of high Sn PVSCs under ambient conditions.

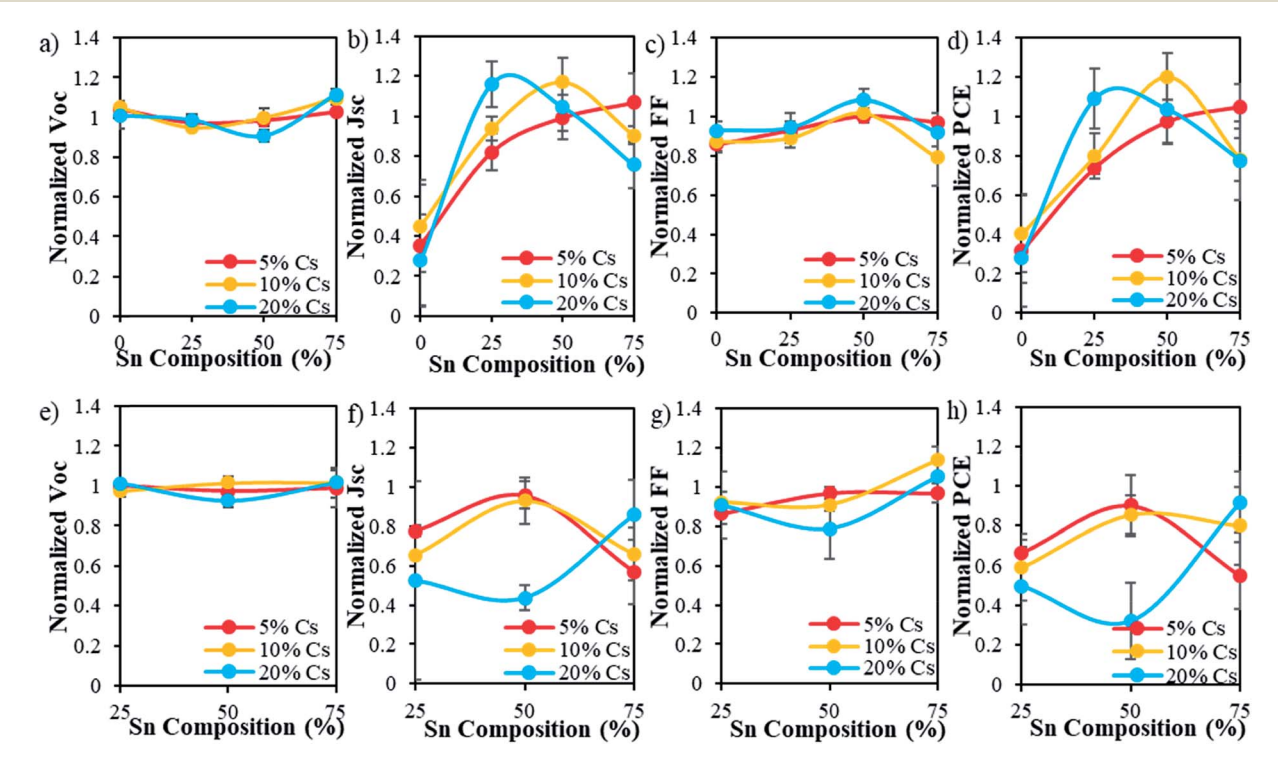


Fig. 6 Normalized (a and e) V_{oc} , (b and f) J_{sc} , (c and g) FF, and (d and h) PCE for unencapsulated PVSCs as a function of Sn composition for each Cs under inert conditions after 30 days (a, b, c and d) and after an additional 5 days under ambient conditions (e, f, g and h).

Conclusions

In summary, for the first time the optimized triple cation Cs/FA/ MA and double halide Br/I compositions were applied to Pb-Sn alloyed perovskites $Cs_x(MA_{0.17}FA_{0.83})_{1-x}Pb_{1-y}Sn_y(I_{0.83}Br_{0.17})_3$. The synthesized perovskite films were smooth, dense and showed a pure cubic α-phase with high crystallinity. The MX₆ octahedral tilting and lattice constriction from the compositional tuning resulted in a nonlinear lattice trend for the Pb-Sn alloyed perovskites as well as the opposite band gap trends in the Pb-rich or Sn-rich perovskites with the increase of Cs for fixed Sn compositions. The corresponding devices achieved high efficiency on a PEDOT:PSS inverted architecture with a PCEmax of 15.78% for the $Cs_{0.10}(MA_{0.17}FA_{0.83})_{0.90}Pb_{0.75}Sn_{0.25}(I_{0.83}Br_{0.17})_3$ PVSC and a record high PCE_{max} of 11.05% for the high Sn $Cs_{0.05}(MA_{0.17}FA_{0.83})_{0.95}Pb_{0.25}Sn_{0.75}(I_{0.83}Br_{0.17})_3$ PVSC. Adding Cs to the triple cation Cs/MA/FA, mixed halide Br/I Pb-Sn alloyed perovskites suppressed the yellow phase and Sn⁴⁺ impurities, creating highly uniform and crystalline perovskite films that can retain ~80% of their initial PCE for 30 days under inert conditions followed by 5 days under ambient condition with a relatively humidity of 35 \pm 5%. Overall, this study demonstrated the implementation of the triple cation, double halides as an effective strategy for improving the performance and stability of high Sn PVSCs, providing a route towards lead-free devices in the future.

Experimental

Materials

Lead(II) iodide (PbI₂, 99%), tin(II) iodide (SnI₂, 99.99%), lead(II) bromide (PbBr₂, 99.999%), cesium iodide (CsI, 99.999%), tin(II) fluoride (SnF₂ 99%), toluene (anhydrous, 99.8%), chloroform (\geq 99.99%), γ -butyrolactone (GBL, \geq 99%), N,N-dimethyl sulfoxide (DMSO, anhydrous, \geq 99.9%), and bathocuproine (BCP, 96%) were purchased from Sigma-Aldrich (St. Louis, Missouri) and used without further purification. Methylammonium iodide (MAI), formamidinium iodide (FAI), and formamidinium bromide (FABr) were purchased from Greatcell Solar (Queanbeyan, Australia) without further purification. The PC₆₀BM (>99.5%) and C₆₀ (>99.5%) were purchased from American Dye Source (Quebec, Canada).

Perovskite thin film fabrication

The perovskite precursor solutions were prepared by dissolving MAI, FAI, PbI₂, PbBr₂, SnI₂, and FABr at the corresponding molar ratios in GBL and DMSO (volume ratio 7 : 3) with a total concentration of 2.5 M. A 10% SnF₂ per molar weight of SnI₂ was added to the precursor solution as a reducing agent. CsI was dissolved in DMSO at a concentration of 1.5 M and added to the precursor to achieve the correct triple cation composition. The precursors were mixed at 60 °C for 1 h and were filtered through a 0.2 μm PTFE filter before use. Plain glass was cut into 15 mm \times 15 mm substrates which were then cleaned νia ultrasonication for 15 min in detergent in Millipore deionized water, acetone, and isopropanol in sequence. The substrates

were treated with oxygen plasma under 100 W for 10 min. A 70 μ L drop of precursor solution was spin-coated on a cleaned glass substrate at 500 rpm for 5 s, 1000 rpm for 15 s, and 4000 rpm for 40 s in a nitrogen glove box. A toluene anti-solvent was *in situ* dripped onto the substrate during the last 15 s of the third spin-coating step. The volume of the anti-solvent was decreased from 800 to 700, 600, 500, and 500 μ L for $Cs_x(MA_{0.17}FA_{0.83})_{1-x}Pb_{1-y}Sn_y(I_{0.83}Br_{0.17})_3$ perovskites with y=0, 0.25, 0.5, 0.75 and 1.0, respectively. The perovskite films were then thermally annealed at 100 °C for 10 min.

Film characterization

Scanning electron microscopy (SEM) and energy dispersive spectroscopy (EDS) were acquired using a FEI Sirion SEM operated at 5 kV and 15 kV to determine the surface morphology and elemental compositions of perovskite thin films, respectively. Two-dimensional X-ray diffraction (XRD) patterns were collected with a Bruker GADDS D8 Focus Powder Discover diffractometer using Cu K α radiation ($\lambda = 1.5419 \text{ Å}$) and the data were processed using the EVA package provided by Bruker Axs to investigate the crystalline structures of perovskite thin films. Ultraviolet-visible (UV-Vis) absorption spectra were collected using a Varian Cary 5000 UV-Vis-NIR spectrophotometer. Photoluminescence (PL) spectra were obtained with a modified Horiba LabRAM HR-800 with 532 nm laser excitation and a Czerny-Turner monochromator blazed at 1200 nm. Measurements were conducted at 1 Sun above the band gap equivalent photon flux with a 532 nm cw laser. The PL experiments were conducted in a N2-filled KF flange with a borosilicate glass window.

Device fabrication

ITO coated glass substrates (10 ohm sq⁻¹ ITO, Colorado Concept Coatings LLC) were cut and cleaned as described above. The PEDOT:PSS (Al 4083, Heraeus CleviosTM) solution was filtered with a 0.45 µm nylon filter. A 70 µL drop of PEDOT:PSS was spin-coated on a cleaned ITO coated glass substrate at 5000 rpm for 60 s and annealed at 150 °C for 10 min in air. The substrates were transferred to a glove box and the perovskite thin films were fabricated as described above. A PC₆₀BM solution (15 mg ml⁻¹ in chloroform) was then spin coated on the perovskite films at 4000 rpm for 60 s and dried without annealing. The substrates were loaded into a thermal evaporation chamber to thermally deposit 20 nm of C₆₀ and 8 nm of BCP. Finally, a mask with 3.14×10^{-6} m² area holes was placed on devices to evaporate 150 nm of silver for electrodes in a high vacuum evaporator ($<1 \times 10^{-6}$ torr). The resulting device structure is ITO/PEDOT:PSS/perovskite/PC₆₀BM/C₆₀/BCP/Ag.

Device characterization

The photocurrent density-voltage (J-V) curve measurements were conducted in a N_2 glovebox with a Keithley 2400 Source Meter and a Solar Light Co. Xenon lamp (16S-300 W) and an AM 1.5 filter. Before measurements, the light intensity was calibrated to 100 mW cm $^{-2}$ using a standardized National Renewable Energy Laboratory calibrated silicon solar cell. EQE

measurements were performed under ambient conditions without encapsulation using a xenon lamp (Oriel, 450 W) light source, a monochromator (Newport Cornerstone 130), an optical chopper, a lock-in amplifier (Stanford Research Corp SR830), and finally a NIST-certified Si-photodiode (Thorlabs FDS 100-CAL) for calibration.

Conflicts of interest

Paper

The authors declare no conflict of interest.

Acknowledgements

This work was supported by the National Science Foundation (NSF) (CBET-1748101 and CMMI-1661660). GAT acknowledges the support from the NSF Graduate Research Fellowship Program Fellowship and the University of Washington (UW) Clean Energy Institute (CEI) Graduate Research and Education Fellowships funded by the State of Washington via the Washington Research Foundation. Part of this work was conducted at the Molecular Analysis Facility, a National Nanotechnology Coordinated Infrastructure site at the UW which is supported in part by the NSF (ECC-1542101), the UW, the Molecular Engineering & Sciences Institute, the CEI, and the National Institutes of Health. Some device fabrications were carried out in the UW Department of Chemistry's Photonics Research Center. UV-Vis-NIR absorption measurements were carried out in the UW Department of Chemistry's Spectroscopic and Analytical Instrumentation facility. EQE and photoluminescence measurements were conducted in the labs of Professors Alex Jen and Hugh Hillhouse, respectively.

Notes and references

- 1 A. Kojima, K. Teshima, Y. Shirai and T. Miyasaka, J. Am. Chem. Soc., 2009, 131, 6050.
- 2 M. Saliba, T. Matsu, J. Y. Seo, K. Domanski, J. P. Correa-Baena, M. K. Nazeeruddin, S. M. Zakeeruddin, W. Tress, A. Abate, A. Hagfeldt and M. Grätzel, Energy Environ. Sci., 2016, 9, 1989.
- 3 M. Lee and H. Snaith, Science, 2012, 338, 643.
- 4 J. H. Heo, D. H. Song and S. H. Im, Adv. Mater., 2014, 26,
- 5 P. Prajongtat and T. Dittrich, J. Phys. Chem. C, 2015, 119,
- 6 F. Hao, C. C. Stoumpos, D. H. Cao, R. P. H. Chang and M. G. Kanatzidis, Nat. Photonics, 2014, 8, 489.
- 7 S. D. Stranks, G. E. Eperon, G. Grancini, C. Menelaou, M. J. P. Alcocer, T. Leijtens, L. M. Hertz, A. Petrozza and H. J. Snaith, Science, 2013, 342, 341.
- 8 A. Miyata, A. Mitioglu, P. Piochocka, O. Portugall, J. T. W. Wang, S. D. Stranks, H. J. Snaith and R. J. Nicholas, Nat. Photonics, 2015, 11, 582.
- 9 C. Wehrenfennig, G. E. Eperon, M. B. Johnston, H. J. Snaith and L. M. Herz, Adv. Mater., 2014, 26, 1584.
- 10 M. A. Green, A. Ho-Baillie and H. J. Snaith, Nat. Photonics, 2014, 8, 506.

- 11 B. Conings, J. Drijkoningen, N. Gauquelin, A. Babayigit, J. D'Haen, L. D'Olieslaeger, Aa. Ethirajan, J. Verbeeck, J. Manca, E. Mosconi, F. De Angelis and H. G. Boyen, Adv. Energy Mater., 2015, 5, 1.
- 12 C. Stoumpos, C. D. Malliakas and M. Kanatzidis, Inorg. Chem., 2013, 52, 9019.
- 13 J. A. Christians, P. A. M. Herrera and P. V. Kamat, J. Am. Chem. Soc., 2015, 137, 1530.
- 14 R. L. Z. Hoye, P. Schulz, L. T. Schelhas, A. M. Holder, K. H. Stone, J. D. Perkins, D. Vigil-Fowler, S. Siol, D. O. Scanlon, A. Zakutayeu, A. Walsh, I. C. Smith, B. C. Melot, R. C. Kurchin, Y. Wang, J. Shi, F. C. Marques, J. J. Berry, W. Tumas, S. Lany, V. Stevanovic, M. F. Toney and T. Buonassisi, Chem. Mater., 2017, 29, 1964.
- 15 Z. Li, M. Yang, J.-S. Park, S.-H. Wei, J. J. Berry and K. Zhu, Chem. Mater., 2015, 28, 284.
- 16 G. E. Eperon, G. M. Paterno, R. J. Sutton, A. Zampetti, A. A. Haghighirad, F. Cacialli and H. J. Snaith, J. Mater. Chem., 2014, 3, 19688.
- 17 R. J. Sutton, G. E. Eperon, L. Miranda, E. S. Parrott, B. A. Kamino, J. B. Patel, M. T. Horantner, M. B. Johnston, A. A. Haghighirad, D. T. Moore and H. J. Snaith, Adv. Energy Mater., 2016, 6, 1.
- 18 D. P. McMeekin, G. Sadoughi, W. Rehman, G. E. Eperon, M. Saliba, M. T. Horantner, A. Haghighirad, N. Sakai, L. Korte, B. Rech, M. B. Johnston, L. M. Hertz and H. J. Snaith, Science, 2016, 351, 151.
- 19 D. Bi, W. Tress, M. I. Dar, P. Gao, J. Luo, C. Renevier, K. Schenk, A. Abate, F. Giordano, J. P. Correa-Baena, J. D. Decoppet, S. M. Zakeeruddin, M. K. Nazeeruddin, M. Grätzel and A. Hagfeldt, Sci. Adv., 2016, 2, 1.
- 20 M. Saliba, S. Orlandi, T. Matsui, S. Aghazada, M. Cavazzini, J. P. Correa-Baena, P. Gao, R. Scopelliti, E. Mosconi, K. H. Dahmen, F. De Angelis, A. Abate, A. Hagfeldt, G. Pozzi, M. Grätzel and M. K. Nazeeruddin, Nat. Energy, 2016, 1, 1.
- 21 Y. Wang, J. Wu, P. Zhang, D. Liu, T. Zhang, L. Ji, X. Gu, Z. D. Chen and S. Li, Nano Energy, 2017, 39, 616.
- 22 S. Chatterjee and A. J. Pal, J. Mater. Chem., 2018, 6, 3793.
- 23 Q. Chen, N. De Marco, Y. M. Yang, T. B. Song, C. C. Chen, H. Zhao, Z. Hong, H. Zhou and Y. Yang, Nano Today, 2015,
- 24 X. Liu, Z. Yang, C. C. Chen, A. Rajagopal, S. T. Williams, Y. Sun and A. K. Y. Jen, J. Mater. Chem., 2015, 4, 17939.
- 25 Y. Ogomi, A. Morita, S. Tsukamoto, T. Saitho, N. Faujikawa, G. Shen, T. Toyoda, K. Yoshino, S. S. Pandey, T. Ma and S. Hayase, J. Phys. Chem. Lett., 2014, 5, 1004.
- 26 F. Hao, C. C. Stoumpos, R. P. H. Chang and M. G. Kanatzidis, J. Am. Chem. Soc., 2014, 136, 8094.
- 27 Z. Yang, A. Rajagopal and A. K.-Y. Jen, Adv. Mater., 2017, 29,
- 28 K. Liang, D. B. Mitzi and M. T. Prikas, Chem. Mater., 1998, 10,
- 29 F. Hao, C. C. Stoumpos, P. Guo, N. Zhou, T. J. Marks, R. P. H. Chang and M. G. Kanatzidis, J. Am. Chem. Soc., 2015, 137, 11445.
- 30 Z. Yang, A. Rajagopal, C. C. Chen, S. B. Jo, B. Liu, T. Zhao and A. K. Y. Jen, Adv. Mater., 2016, 28, 8990.

- 31 A. G. Kontos, A. Kaltzoglou, E. Sirandi, D. Palles, G. K. Angeli, M. K. Arfanis, V. Psycharis, Y. S. Raptis, E. I. Kamitsos, P. N. Trikalitis, C. C. Stoumpos, M. G. Kanatzidis and P. Falaras, *Inorg. Chem.*, 2016, 56, 84.
- 32 I. Chung, B. Lee, J. He, R. P. H. Chang and M. G. Kanatzidis, *Nature*, 2012, **485**, 486.
- 33 S. J. Lee, S. S. Shin, Y. C. Kim, D. Kim, T. K. Ahn, J. H. Noh, J. Seo and S. I. Seok, *J. Am. Chem. Soc.*, 2016, **138**, 3974.
- 34 W. Liao, D. Zhao, Y. Yu, C. R. Grice, C. Wang, A. J. Cimaroli, P. Schulz, W. Meng, K. Zhu, R. G. Xiong and Y. Yan, *Adv. Mater.*, 2016, 28, 9333.
- 35 N. J. Jeon, J. H. Noh, Y. C. Kim, W. S. Yang, S. Ryu and S. I. Seok, *Nat. Mater.*, 2014, **13**, 897.
- 36 F. Hao, C. C. Stoumpos, P. Guo, N. Zhou, T. J. Marks, R. P. H. Chang and M. G. Kanatzidis, *J. Am. Chem. Soc.*, 2015, 137, 11445.
- 37 E. J. Zheng, B. Yuh, G. A. Tosado and Q. M. Yu, *J. Mater. Chem. C*, 2017, 5, 3796.
- 38 L. Z. Zhu, B. Yuh, S. Schoen, X. Li, M. Aldighaithir, B. J. Richardson, A. Alamer and Q. M. Yu, *Nanoscale*, 2016, 8, 7621.
- 39 F. Ma, J. Li, W. Li, N. Lin, L. Wang and J. Qiao, *Chem. Sci.*, 2016, **8**, 800.
- 40 J. Liang, C. Wang, P. Zhao, Z. Lu, Y. Ma, Z. Xu, Y. Wang, H. Zhu, Y. Hu, G. Zhu, L. Ma, C. Tao, Z. Tie, J. Liu and Z. Jin, *Nanoscale*, 2016, 9, 11841.
- 41 C. Yi, J. Luo, S. Meloni, A. Boziki, N. Ashari-Astani, C. Grätzel, S. M. Zakeeruddin, U. Rothlisberger and M. Grätzel, *Energy Environ. Sci.*, 2015, 9, 656.
- 42 M. Deepa, M. Salado, L. Calio, S. Kazim, S. M. Shivaprasad and S. Ahmad, *Phys. Chem. Chem. Phys.*, 2016, **19**, 4069.

- 43 V. Goldschmidt, Sci. Nat., 1926, 14, 477.
- 44 G. Kieslich, S. Sun and A. K. Cheetham, *Chem. Sci.*, 2014, 6, 3430.
- 45 B. Saparov and D. B. Mitzi, Chem. Rev., 2016, 116, 4558.
- 46 W. Travis, E. N. K. Glover, H. Bronstein, D. O. Scanlon and R. G. Palgrave, *Chem. Sci.*, 2015, 7, 4548.
- 47 J.-W. Lee, D.-H. Kim, H.-S. Kim, S.-W. Seo, S. M. Cho and N.-G. Park, *Adv. Energy Mater.*, 2015, **5**, 1501310.
- 48 R. Prasanna, A. Gold-Parker, T. Leijtens, B. Conings, A. Babayigit, H. G. Boyen, M. F. Toney and M. D. McGhee, J. Am. Chem. Soc., 2017, 139, 11117.
- 49 J. H. Lee, N. C. Bristowe, J. H. Lee, S. H. Lee, P. D. Bristowe, A. K. Cheetham and H. M. Jang, *Chem. Mater.*, 2016, 28, 4259.
- 50 C. Ferrara, M. Patrini, A. Pisanu, P. Quadrelli, C. Milanese, C. Tealdi and L. Malavasi, *J. Mater. Chem.*, 2016, 5, 9391.
- 51 Y. Shao, Z. Xiao, C. Bi, Y. Yuan and J. Huang, *Nat. Commun.*, 2014, 5, 5784.
- 52 Z. Xiao, C. Bi, Y. Shao, Q. Dong, Q. Wang, Y. Yuan, C. Wang, Y. Gao and J. Huang, *Energy Environ. Sci.*, 2013, 7, 2619.
- 53 M. Konstantakou and T. Stergiopoulos, *J. Mater. Chem.*, 2016, 5, 11518.
- 54 H. J. Snaith, A. Abate, J. M. Ball, G. E. Eperon, T. Leijtens, N. K. Noel, S. D. Stranks, J. T. W. Wang, K. Wojciechowski and W. Zhang, *J. Phys. Chem. Lett.*, 2014, 5, 1511.
- 55 E. L. Unger, E. T. Hoke, C. D. Bailie, W. H. Nguyen, A. R. Bowring, T. Heumuller, M. G. Christoforo and M. D. McGhee, *Energy Environ. Sci.*, 2013, 7, 3690.
- 56 M. M. Tavakoli, S. M. Zakeeruddin, M. Grätzel and Z. Fan, *Adv. Mater.*, 2018, **30**, 1705998.